Uludağ University Journal of The Faculty of Engineering, Vol. 31, No. 1, 2026 RESEARCH

DOI: 10.17482/uumfd.1796644

EVALUATION OF DEFLECTION PERFORMANCE OF SIZING-OPTIMIZED COLD-FORMED STEEL BEAMS WITH VARIOUS CROSS-SECTIONS

Semih KONCELİ [*]
Gökhan GÜÇLÜ [*]
Uğur KAFKAS [**]

Received: 03.10.2025; revised: 06.11.2025; accepted: 29.12.2025

Abstract: Strength-based optimization of cold-formed steel (CFS) sections is a common strategy to enhance material efficiency, but it often results in slender profiles where serviceability performance is a concern. This study investigates the deflection performance of three distinct CFS profiles—a lipped channel, an unlipped channel, and a built-up I-section—after they were sizing-optimized (via parametric scaling) for strength limit states according to AISI S100-16. The final optimized dimensions for both secondary beams and girders were evaluated against the serviceability criteria of the International Building Code. A numerical analysis based on the conjugate beam method was employed, which accurately accounts for the variable effective moment of inertia along the beams' spans. The results demonstrate that all six optimized sections comfortably satisfy the deflection limits for both live load (L) and total load $(D+L)$ conditions. A comparative analysis revealed that while the lipped channel section was the most materially efficient, it exhibited greater, though still acceptable, deflections compared to the heavier unlipped and I-sections. This study contributes by quantitatively demonstrating that CFS beams optimized solely for AISI S100-16 strength limits can inherently satisfy IBC serviceability criteria, confirming the viability of this optimization approach in practical floor design. The findings confirm that a well-executed strength optimization does not compromise serviceability and that the lipped channel section provides an optimal balance between material economy and structural performance for the floor system studied.

Keywords: Cold-Formed Steel, Deflection, Serviceability Limit State, Section Optimization, Effective Moment of Inertia

Çeşitli Enkesitli Boyut Optimizasyonu Yapılmış Soğukta Şekil Verilmiş Çelik Kirişlerin Sehim Performansının Değerlendirilmesi

Öz: Soğukta şekil verilmiş çelik (SŞVÇ) kesitlerin dayanım esaslı optimizasyonu, malzeme verimliliğini artırmak için yaygın bir stratejidir, ancak bu durum genellikle kullanılabilirlik performansının kritik hale geldiği narin profillerle sonuçlanır. Bu çalışma, AISI S100-16'ya göre dayanım sınır durumları için (parametrik ölçeklendirme yoluyla) boyut optimizasyonu yapıldıktan sonra üç farklı SŞVÇ profilinin—dudaklı C, dudaksız C ve birleşik I-kesit—sehim performansını incelemektedir. Hem tali kirişler hem de ana kirişler için optimizasyon sonucu elde edilen boyutlar, Uluslararası Yapı Yönetmeliği'nin kullanılabilirlik kriterlerine göre değerlendirilmiştir. Kirişlerin açıklıkları boyunca değişken olan etkin atalet momentini hassas bir şekilde hesaba katan, eşlenik kiriş yöntemine dayalı sayısal bir analiz gerçekleştirilmiştir. Sonuçlar, altı optimize edilmiş kesitin tamamının hem hareketli yük (L) hem de toplam yük $(D+L)$ koşulları için sehim sınırlarını rahatlıkla sağladığını göstermektedir. Yapılan karşılaştırmalı analizde, dudaklı C kesitinin malzeme açısından en verimli olmasına rağmen, daha ağır

[*] Department of Civil Engineering, Engineering Faculty, Kütahya Dumlupınar University, 43100 Kütahya, Türkiye
[**] Department of Construction Technology, Vocational School of Technical Science, Kütahya Dumlupınar University, 43100 Kütahya, Türkiye

Corresponding Author: Gökhan Güçlü (gokhan.guclu@dpu.edu.tr)

olan dudaksız C ve I-kesitlere kıyasla daha büyük, ancak yine de kabul edilebilir, sehimler oluşturduğu görülmüştür. Bu çalışma, yalnızca AISI S100-16 dayanım sınırlarına göre optimize edilmiş SŞVÇ kirişlerin, IBC kullanılabilirlik kriterlerini kendiliğinden karşılayabildiğini kantitatif olarak göstererek bu optimizasyon yaklaşımının pratik döşeme tasarımındaki uygulanabilirliğini doğrulamaktadır. Bulgular, etkin bir dayanım optimizasyonunun kullanılabilirliği tehlikeye atmadığını ve dudaklı C kesitinin, incelenen döşeme sistemi için malzeme ekonomisi ve yapısal performans arasında en uygun dengeyi sağladığını doğrulamaktadır.

Anahtar Kelimeler: Soğukta Şekil Verilmiş Çelik, Sehim, Kullanılabilirlik Sınır Durumu, Kesit Optimizasyonu, Etkin Atalet Momenti

1. INTRODUCTION

Cold-formed steel (CFS) construction has become a cornerstone of modern building practices, offering a compelling alternative to traditional materials like hot-rolled steel, concrete, and timber (AbouHamad and Abu-Hamd, 2019; Thirunavukkarasu et al., 2021). Its rising prominence is attributable to a unique combination of advantages, including a high strength-to-weight ratio, exceptional durability, and inherent non-combustibility (Liang et al., 2022; Sheta et al., 2021). From a sustainability perspective, CFS is highly favored due to its significant potential for recycling and reuse, which aligns with the principles of a circular economy and reduces the environmental footprint of construction projects (AbouHamad and Abu-Hamd, 2019; Marrone et al., 2023; Tavares et al., 2021). The prefabrication capabilities of CFS components facilitate modular construction, leading to accelerated project timelines, improved quality control, and reduced on-site labor demands (Thirunavukkarasu et al., 2021; Lawson and Richards, 2010). These attributes make CFS an efficient and sustainable solution for a wide range of applications, from residential and commercial framing to industrial buildings and modular systems (Schafer, 2011; Rukavina et al., 2022).

Despite these benefits, the design of CFS members presents unique engineering challenges. The use of thin steel sheets makes the sections susceptible to various buckling phenomena—namely local, distortional, and global (flexural-torsional) buckling—which often occur at stress levels well below the material's yield strength (Ádány et al., 2008; Peng et al., 2025). These instability modes are critical as they can significantly reduce both the load-carrying capacity (strength) and the bending stiffness of the member (Ayhan and Schafer, 2015; Rasmussen, 2023). Consequently, a comprehensive design must address not only the Ultimate Limit States (ULS), which govern structural safety and collapse prevention, but also the Serviceability Limit States (SLS), which pertain to functional performance under normal service conditions (Mojtabaei et al., 2021a; Mojtabaei et al., 2019). Among the serviceability criteria, controlling deflection is particularly critical, as excessive vertical displacement can damage non-structural elements, create aesthetic problems, and impair the overall functionality of a building (Gossen, n.d.; Lim and Nethercot, 2003; Phan et al., 2013).

The inherent flexibility in the manufacturing process of CFS profiles provides a unique opportunity for structural optimization. By altering the geometry of a cross-section—such as the dimensions of the web, flanges, and lips, or by introducing new stiffeners—it is possible to significantly enhance its structural performance without increasing the amount of material used (Ye et al., 2016a; Leng et al., 2011). This has spurred extensive research into shape and size optimization, with the primary goal of maximizing member strength by delaying the onset of buckling. Various computational intelligence techniques, including genetic algorithms (Parastesh et al., 2021; Parastesh et al., 2019; Mojtabaei et al. 2021b), particle swarm optimization (Ye et al., 2016b; Fourie and Groenwold, 2002; Gatheeshgar et al., 2020), and the method of moving asymptotes (Svanberg, 1987), have been successfully employed to explore vast design spaces and identify novel, high-performance cross-sections. These optimization studies have consistently demonstrated that tailored CFS profiles can offer substantial capacity

improvements over standard, commercially available shapes (Ye et al., 2016a; Phan et al., 2020; Leng et al., 2011).

However, an optimization strategy focused solely on maximizing strength often produces highly slender and geometrically complex profiles. While these sections are efficient from a ULS perspective, their reduced thickness and optimized shapes can lead to lower bending stiffness, raising significant concerns about their performance under service loads (Akchurin et al., 2022; Akchurin et al., 2023). This creates a fundamental tension between strength and stiffness in CFS design (Gossen, n.d.). The effective bending stiffness of a CFS member is not constant; it diminishes as compressive stresses increase due to the effects of local and distortional buckling, a phenomenon accounted for by using an effective moment of inertia (I_{eff}) (Ayhan and Schafer, 2015; Rasmussen, 2023). Accurately predicting this variable stiffness is crucial for calculating deflections, yet it poses a considerable analytical challenge (Ayhan and Schafer, 2015; Ayhan and Schafer, 2012). While design standards like the American Iron and Steel Institute's AISI S100 (American Iron and Steel Institute, 2022) provide methodologies such as the Effective Width Method (EWM) and the Direct Strength Method (DSM) to determine member strength (Mahar et al., 2022; Schafer, 2019), the direct application of these principles to serviceability checks requires careful implementation, especially for optimized sections where stiffness reductions may be more pronounced (Akchurin et al., 2022; Akchurin et al., 2023).

The existing body of literature reflects this dual focus on strength and serviceability. Numerous studies have successfully developed optimized sections for ULS criteria, demonstrating significant gains in flexural and compressive strength for single sections (Parastesh et al., 2019; Phan et al., 2020; Ye et al., 2016b), built-up members (Phan and Rasmussen, 2019; Deng et al., 2022; Rasmussen et al., 2025), and members with perforations (Ananthi et al., 2024; Abdel-Rahman and Sivakumaran, 1998). Concurrently, other research has highlighted the critical need to integrate SLS constraints into the optimization process. For instance, Mojtabaei et al. (2021a), Mojtabaei et al. (2019) developed a framework for optimizing CFS beams for both ULS and SLS requirements according to Eurocode 3, showing that different cross-sectional shapes are optimal depending on whether strength or deflection is the governing criterion. Similarly, Akchurin et al. (2022) and Akchurin et al. (2023) advanced optimization schemes for lipped channel sections that incorporate both strength and stiffness constraints, concluding that an optimized family of sections can replace a much larger set of standard profiles while maintaining performance for both limit states. These studies confirm that a design is not truly optimal unless it satisfies both strength and serviceability requirements.

While previous research has established the importance of considering both ULS and SLS, a gap remains in understanding the practical serviceability performance of sections that have been aggressively optimized solely for strength. A strength-first optimization pushes a design to its material efficiency limit, resulting in the most slender, and therefore most deflection-susceptible, profile possible. A critical question for designers is whether such a highly efficient section retains sufficient stiffness to meet stringent deflection limits in a realistic structural system, such as a floor. This study addresses this practical concern by first performing a rigorous strength-based optimization of three common CFS profiles—a lipped channel, an unlipped channel, and a built-up I-section—for both secondary beams and girders in a typical composite floor system. The optimization is carried out to satisfy the strength limit states specified in AISI S100-16. Subsequently, the deflection performance of these optimized, slender sections is thoroughly evaluated against the serviceability criteria of the International Building Code (IBC) (International Codes Council, 2018). To ensure accuracy, the deflection analysis employs a numerical procedure based on the conjugate beam method, which explicitly accounts for the variable effective moment of inertia along the member span. By systematically optimizing for strength and then verifying for serviceability, this work investigates whether a design pushed to its ultimate strength capacity can inherently satisfy functional performance

requirements, thereby providing valuable insights into the efficiency and viability of optimized CFS sections in practical applications.

2. MATERIALS AND METHODS

2.1. Structural System and Loads

The structural system analyzed in this study is a 6000 mm × 6000 mm composite floor system designed for residential or office use. The system consists of secondary beams with a 6000 mm span, which are spaced at 1500 mm on center and supported by the girders (see Figure 1). The secondary beams are simply supported by the girders, and the girders are simply supported by the columns.

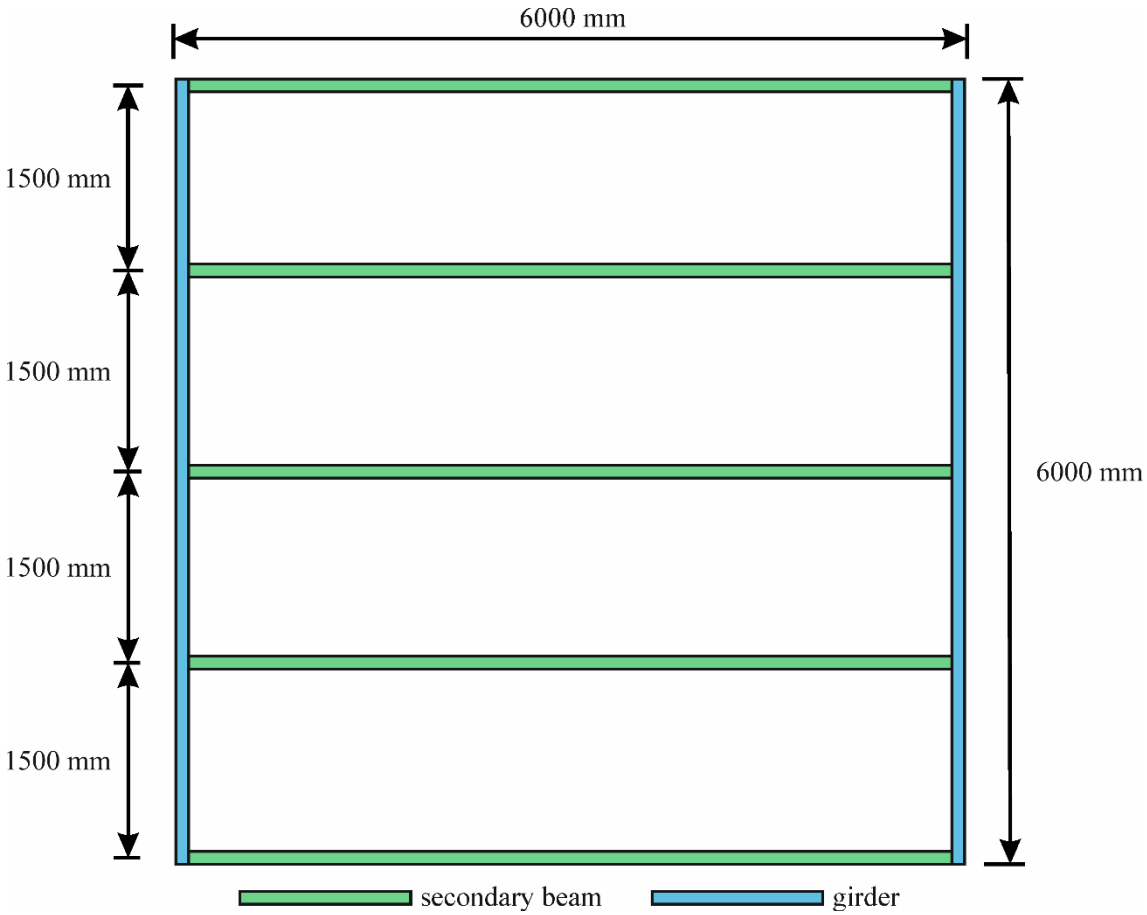

Figure 1:
Plan layout of the composite floor system

The design loads consist of dead loads (D) and live loads (L). The dead load comprises the calculated self-weight of the steel members—determined using a specific weight of 76 kN/m^3 (American Society for Testing and Materials, 2019)—plus superimposed loads from the floor assembly. These superimposed loads include a 75 mm thick concrete slab (1.8 kN/m^2) (İnşaat Mühendisleri Odası, 2017), a trapezoidal steel deck (0.036 kN/m^2) (Özçe Demir Çelik, n.d.), and an allowance for finishing materials and mortar (1.1 kN/m^2) (Celep, 2022). The live load for residential and office applications was taken as 1.96 kN/m^2 in accordance with the TS 498 standard (Türk Standartları Enstitüsü, 2024).

All analyses were performed using the Load and Resistance Factor Design (LRFD) method as stipulated in the AISI S100-16 specification. The load combinations for the LRFD method were established in accordance with the ASCE/SEI 7-22 specification (American Society of Civil Engineers, 2022). As the beams are internal structural members not exposed to environmental loads, two primary load combinations consisting of dead and live loads were considered in the strength calculations: $1.4D$ and $1.2D+1.6L$.

2.2. Cross-Section Profiles and Optimization Criteria

Three cold-formed steel profiles commonly employed in the construction industry were selected for this study: a lipped channel (lipped C-section), an unlipped channel (unlipped C-section), and a built-up I-section (back-to-back unlipped C-section), as shown in Figure 2.

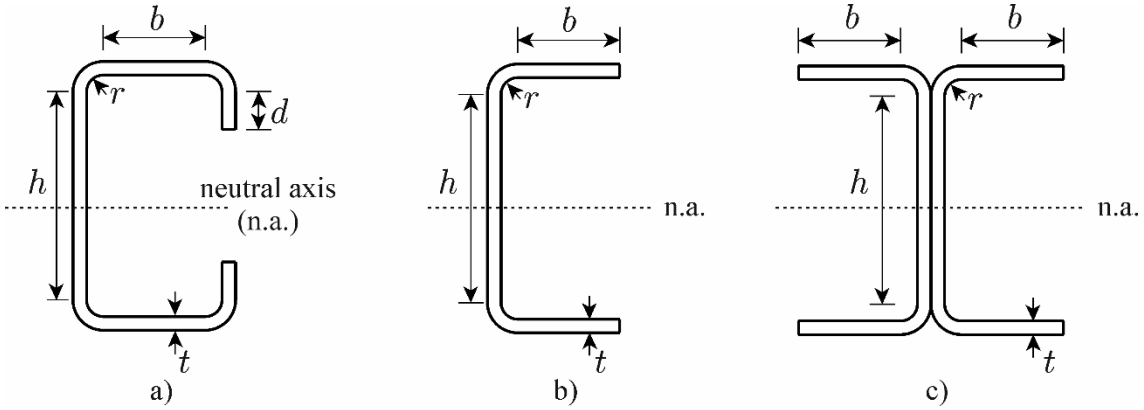

Figure 2:
Cross-section profiles investigated in the study: a) Lipped channel, b) Unlipped channel, c) Built-up I-section

The initial, pre-optimization nominal dimensions of these sections, which served as a baseline for the analysis, are presented in Table 1. These dimensions were chosen as they represent typical profiles used in practice for similar spans and loading conditions.

Table 1. Pre-optimization dimensions of the cross-sections

Profile Type	b (mm)	h (mm)	d (mm)	r (mm)	t (mm)
Lipped channel	70	300	20	2.5	2.5
Unlipped channel	70	300	0	2.5	2.5
Built-up I-section	70	300	0	2.5	2.5

The optimization procedure was applied independently to all three cross-section profiles for both secondary beams and girders, resulting in a total of six unique design cases. The design of each case was governed by the criteria specified in the AISI S100-16 specification. The AISI S100-16 specification provides several design philosophies (load and resistance factor design, allowable strength design, limit states design). To calculate the nominal member strength required by these philosophies, the specification allows for two primary analytical methods: the effective width method and the direct strength method. For this study, the effective width method was utilized for all strength calculations. The analysis accounted for a comprehensive set of strength limit states, including flexural failure modes (yielding, lateral-torsional buckling, local buckling, and distortional buckling), shear failure modes (shear yielding and web elastic shear buckling), and the interaction of combined bending and shear.

For each of the six cases, the optimization algorithm iteratively adjusted the section's geometric dimensions. To implement this procedure, a custom script was developed in the MATLAB environment. This adjustment was achieved by applying a uniform scaling factor (α) to all dimensional parameters $(h,b,d,r$ and $t)$ in each step. The process continued until the ratio of the calculated design strength (R_d) to the required strength (R_u) satisfied the following condition: $1 \le R_d / R_u < 1.001$. This criterion ensures that the final profile is both structurally adequate $(R_d / R_u \ge 1)$ and highly efficient by minimizing oversizing within a 0.1% tolerance.

2.3. Deflection Analysis Methodology

Serviceability limit states are design criteria that define the functional performance of a structure under normal service conditions. Unlike strength limit states, which address safety and collapse prevention, serviceability focuses on ensuring the structure performs its intended function effectively and maintains occupant comfort. Key serviceability considerations include deflection, vibration, and component cracking. For flexural members like floor joists and beams, the most critical serviceability criterion is often deflection (Lim and Nethercot, 2003). A design that is perfectly optimized for strength might exhibit excessive deflection under service loads, potentially causing damage to non-structural finishes, creating aesthetic issues, or impairing the building's function. Therefore, a critical question for designers is whether sections pushed to their ultimate strength capacity remain adequately stiff to satisfy serviceability criteria (Akchurin et al., 2022).

Following the strength-based optimization, the final, optimized cross-sections were evaluated for the serviceability limit state of deflection. The deflection calculations were performed according to the principles of AISI S100-16, and the allowable deflection limits were taken from the IBC as $L/360$ for live load and $L/240$ for the combination of dead and live loads.

A key consideration in the analysis of CFS members is that their bending stiffness, represented by the effective moment of inertia (I_{eff}) is not constant along the length of the member. Two primary approaches exist to address this: EWM and the DSM. Under service-level bending moments, the compressive elements of a slender CFS section may experience incipient local buckling, leading to a redistribution of stress away from the central, buckled portion of the element towards the stiffer, unbuckled corners (Rasmussen, 2023). The EWM models this behavior by reducing the geometric contribution of the buckled elements, which results in a cross-section with a lower bending stiffness than that calculated using the full, gross geometry. This reduced stiffness is quantified by the I_{eff} (Bischoff, 2005). A crucial aspect of this phenomenon is that the degree of local buckling, and thus the magnitude of the stiffness reduction, is directly dependent on the level of compressive stress in the element (Ayhan and Schafer, 2012). Since the bending moment and corresponding stresses vary along the length of a beam, the effective moment of inertia is not a constant property but rather a function of the position along the member's span. In regions of high bending moment (e.g., at mid-span), local buckling effects are more pronounced, leading to a greater reduction in stiffness. Conversely, in low-moment regions near the supports, the section behaves as if it were stiffer, with I_{eff} approaching the gross moment of inertia. Accurately predicting the total deflection of a CFS beam therefore requires an integrated approach that accounts for this non-uniform bending stiffness, $EI_{eff}(x)$, along the entire member length. Alternatively, the direct strength method determines the effective stiffness by proportionally reducing the gross moment of inertia of the full cross-section based on the ratio of the member's calculated strength to the applied service moment.

This study utilizes the EWM, following the procedures and equations detailed in AISI S100-16, Appendix 1, where the effective moment of inertia is calculated based on the effective areas of the cross-section's elements that are in compression. To accurately calculate the total deflection under the variable stiffness prescribed by the EWM, a numerical approach based on the conjugate beam method was employed. For this purpose, the beam was discretized into 100 segments, and within each segment, the effective moment of inertia was assumed to vary linearly. Given that the conjugate beam method is a numerical integration of a smooth function (the M / EI diagram), this high-resolution discretization (n=100) provides a numerically stable and converged solution, thus a formal mesh independence study, such as one required for finite element analysis, was deemed unnecessary. The deflection analysis proceeded according to the aforementioned numerical methodology.

The secondary beams, subjected to a uniformly distributed load as shown in Figure 3, were analyzed first.

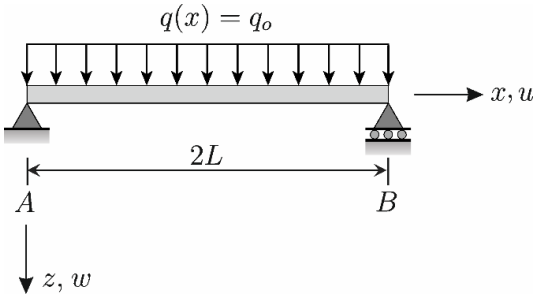

Figure 3:
Secondary beam under uniformly distributed load

Due to the symmetry of both the structural system and the loading about the vertical axis at mid-span, the bending moment and deflection diagrams are symmetric, whereas the shear force diagram is antisymmetric. Consequently, the calculations are performed for only half of the beam span.

The support reactions are given by

$$V_A = -V_B = q_0 L \tag{1}$$

and from the free-body diagram in Figure 4, the bending moment is

$$M(x) = V_A x - \frac{q_0 x^2}{2} = q_0 L x - \frac{q_0 x^2}{2} \tag{2}$$

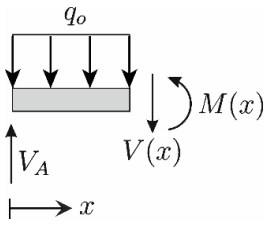

Figure 4:
Free-body diagram for the bending moment calculation in the secondary beam

here, $q_0(x)$ is the magnitude of the unfavorable distributed load obtained from the governing load combination.

The conjugate beam was then loaded with the $M(x)/[EI_{eff}(x)]$ as illustrated in Figure 5. In conjugate beam method, the conjugate beam of a simply supported beam is also a simply supported beam. The loading $M(x)/I_{eff}(x)$ is applied to the conjugate beam as an external distributed load.

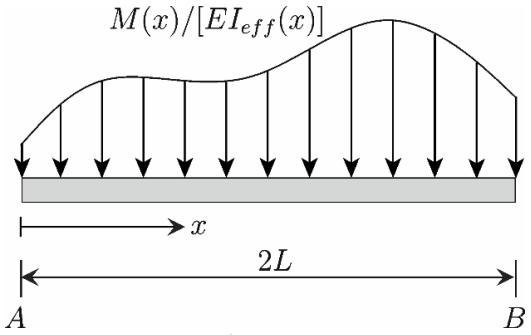

Figure 5:
Conjugate beam for the secondary beam

The moment values obtained from the conjugate beam correspond to the deflection values in the real beam. The division points, along with the support locations, are defined as nodes, resulting in 101 nodes in total $(i=1,2,\ldots,101)$. Due to symmetry, the analysis is performed using only the first 51 nodes, which extend to the mid-span of the beam. The effective moment of inertia (I_{eff}) is calculated with respect to the neutral axis of the effective section. This procedure involves first determining the effective widths of the elements in compression based on the service-level stresses. The neutral axis is then located for this new, reduced-area effective section, and I_{eff} is calculated with respect to this effective neutral axis. This process follows the principles of the Effective Width Method (EWM) as specified in AISI S100-16, Appendix 1. The following notation is used for this process:

$$\begin{aligned} M_1 &\equiv M(x=0), \quad M_2 \equiv M(x=L/50), \quad \ldots \quad M_{51} \equiv M(x=L) \\ I_1 &\equiv I_{eff}(x=0), \quad I_2 \equiv I_{eff}(x=L/50), \quad \ldots \quad I_{51} \equiv I_{eff}(x=L) \end{aligned} \tag{3}$$

The values of M_i (for $i=1,2,\ldots,51$) calculated from eq. (2). The value of I_i (for $i=1,2,\ldots,51$) at each node is then calculated using the corresponding moment value, M_i. It is assumed that the term $M(x)/I_{eff}(x)$ varies linearly between the nodes (see Figure 6).

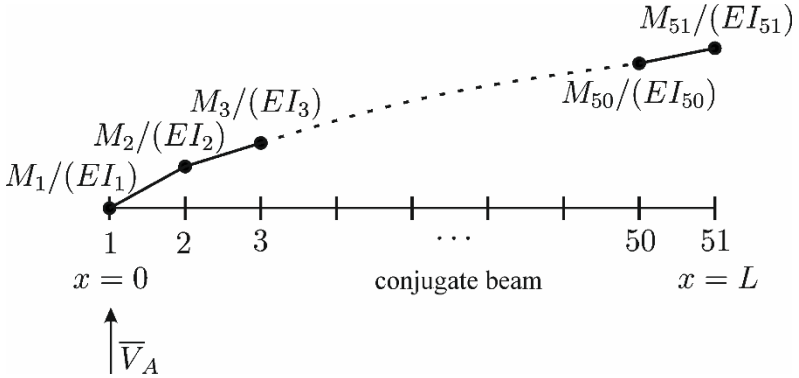

Figure 6:
Assumed variation of $M(x)/(EI_{eff}(x))$ on the conjugate beam

Using the definition:

$$\overline{q}_i = M_i / (EI_i) \tag{4}$$

the reaction force at the left support of the conjugate beam, $\overline{V}_A$, is obtained as (see Figure 6):

$$\overline{V}_A = \sum_{i=1}^{50} \left(\frac{\overline{q}_i + \overline{q}_{i+1}}{2} \right) \frac{L}{50} \tag{5}$$

The geometric properties of the trapezoidal region between nodes i and $i+1$ are obtained as follows (see, Figure 7):

$$\overline{A}_i = \left(\frac{\overline{q}_i + \overline{q}_{i+1}}{2} \right) \frac{L}{50} \tag{6}$$

$$\overline{x}_i = \frac{\overline{q}_i (a/2)(a/3) + \overline{q}_{i+1}(a/2)(2a/3)}{\overline{q}_i (a/2) + \overline{q}_{i+1}(a/2)} = \frac{(\overline{q}_i + 2\overline{q}_{i+1})a}{3(\overline{q}_i + \overline{q}_{i+1})} = \frac{(\overline{q}_i + 2\overline{q}_{i+1})}{3(\overline{q}_i + \overline{q}_{i+1})} \frac{L}{50} \tag{7}$$

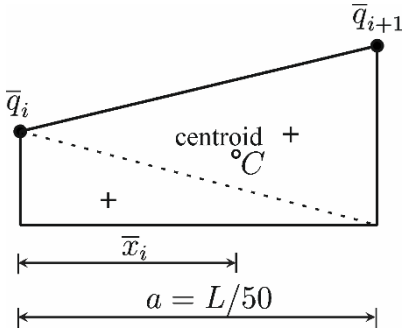

Figure 7:
The segment between the i-th and $(i+1)$-th nodes

The term $\overline{q}_i(x)$ represents the value of the distributed load on the conjugate beam at a local coordinate b_i within a segment, and is determined by linear interpolation:

$$\overline{q}_i(x) = \frac{\overline{q}_{i+1} - \overline{q}_i}{L/50} b_i + \overline{q}_i \tag{8}$$

Using this definition, the area $\overline{\overline{A}}_i$ and centroid $\overline{\overline{x}}_i$ of the sub-segments (see Figure 8) are defined as:

$$\overline{\overline{A}}_i = \left(\frac{\overline{q}_i + \overline{q}_i(x)}{2} \right) b_i \tag{9}$$

$$\overline{\overline{x}}_i = \frac{(2\overline{q}_i + \overline{q}_i(x))}{3(\overline{q}_i + \overline{q}_i(x))} b_i \tag{10}$$

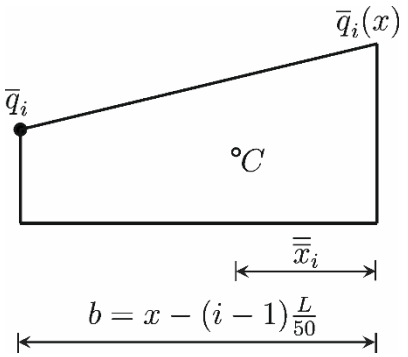

Figure 8:
Definition of variables for a partial segment of the $M/(EI_{eff})$ diagram used in the moment calculation for the conjugate beam

Finally, the moment function, $\bar{M}_i(x)$, at a coordinate x within the interval $(i-1)(L/50) \le x \le (iL)/50$ is obtained as

$$\bar{M}_i(x) = \bar{V}_A\, x - \sum_{j=1}^{i-1}\left(\bar{A}_j\left(x-(j-1)\frac{L}{50}-\bar{x}_j\right)\right) - \bar{\bar{A}}_i\,\bar{\bar{x}}_i \tag{11}$$

for $i = 1,2,\ldots,50$. Eq. (11) defines 50 separate $\bar{M}_i(x)$ functions. The maximum deflection value δ_{max}, is determined from the moment at the mid-span of the conjugate beam:

$$\delta_{\max} = \bar{M}_{max} = \bar{M}_{50}(L) \tag{12}$$

The loading applied to the girder is shown in Figure 9.

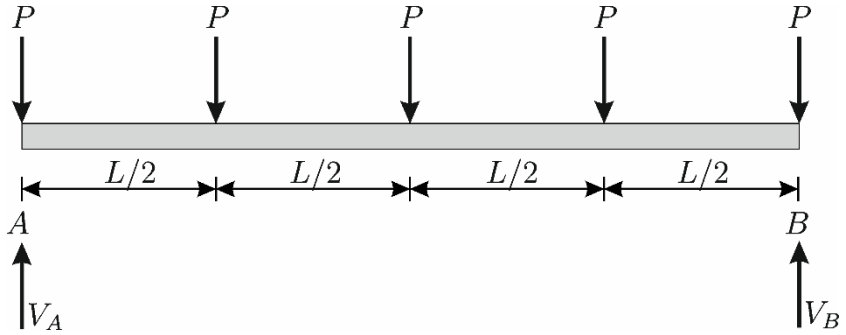

Figure 9:
Loads acting on the girder

For the girder, the support reactions (shear forces) and moment functions are obtained as:

$$V_A = -V_B = 5P/2 \tag{13}$$

$$\begin{aligned} M(x) &= \frac{3P}{2}x, && 0 \le x \le L/2 \\ M(x) &= \frac{P}{2}(x+L), && L/2 < x \le L \end{aligned} \tag{14}$$

The deflection analysis for the girder, which is subjected to point loads as shown in Figure 9, was carried out following the same numerical procedure by using the relevant moment equations.

3. RESULTS AND DISCUSSION

3.1 Optimized Dimensions and Deflection Performance

The strength-based optimization procedure described in the methodology was applied to all three cross-section profiles for both secondary beams and girders. For the secondary beams, the lateral-torsional buckling (LTB) limit state was not considered, as the composite action with the floor slab provides continuous lateral bracing to the compression flange. However, for the optimization of the girders, the LTB strength was calculated and included as a design constraint in accordance with AISI S100-16, as they were considered unbraced during the construction phase. In most cases, the local buckling limit state was found to be the governing criterion that determined the member's design strength. However, for the unlipped channel and built-up I-section girders, the combined bending and shear limit state became the governing criterion. The iterative process yielded six highly efficient cross-sections, and their final optimized dimensions are summarized in Table 2.

Table 2. Optimized cross-section dimensions

Beam Type	Profile Type	α	b (mm)	h (mm)	d (mm)	r (mm)	t (mm)	Cross-section area (mm^2)
Secondary	Lipped channel	1.19	83.4	357.41	23.83	2.98	2.98	1644.87
Secondary	Unlipped channel	1.36	94.86	406.56	-	3.39	3.39	1982.46
Secondary	Built-up I-section	1.08	75.41	323.19	-	2.69	2.69	2505.58
Girder	Lipped channel	1.52	106.59	456.82	30.45	3.81	3.81	2687.19
Girder	Unlipped channel	1.70	119.28	511.22	-	4.26	4.26	3134.53
Girder	Built-up I-section	1.35	94.53	405.12	-	3.38	3.38	3937.03

As established in the methodology, the effective moment of inertia is not constant along the member's span. To illustrate this critical behavior, the variation of I_{eff} was plotted for the built-up I-section girder beam under the total service load $(D+L)$. The normalized curve in Figure 10 is generated by calculating the effective moment of inertia (I_{eff}) at each segment $'x'$ along the beam based on the service-level stress at that point, and then dividing this value by the gross moment of inertia (I_{gross}) of the full cross-section (i.e., I_{eff} / I_{gross}). As shown in Figure 10, the effective moment of inertia remains at its maximum value near the support where the bending moment is low. As the distance from the support increases and the bending moment grows, the effects of local buckling become more pronounced, leading to a gradual reduction in the effective moment of inertia towards the mid-span. The complete nodal data for the effective moment of inertia values for all six cases are provided in Appendix A (for the sake of brevity, these tables present the values only for the odd-numbered nodes).

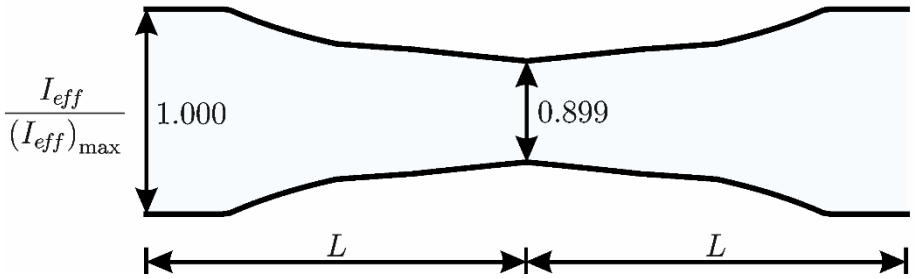

Figure 10:
Normalized variation of the I_{eff} along the full span for the optimized built-up I-section girder under total service load.

Regarding the stiffness reduction shown in Figure 10, the observed maximum reduction of approximately 10% in the effective moment of inertia, while seemingly low for a slender optimized section, is attributed to the applied stress level. The deflection analysis is performed using unfactored service loads $(D+L)$, which induce significantly lower stresses than the factored ultimate loads used for the strength optimization. At these lower service-level stresses, the effects of local buckling are less pronounced, resulting in a more limited, though still critical, reduction in bending stiffness.

Using the numerical procedure described, the final maximum deflection values for all six optimized sections were determined. The calculated deflections were compared against the allowable limits to verify compliance with the serviceability criteria. The results of this final performance check are summarized in Table 3.

Table 3. Deflection performance of optimized sections

Beam Type	Profile Type	Load Case	Allowable Deflection (mm)	Calculated Deflection (mm)	Status
Secondary	Lipped channel	Live Load (L)	16.67 $(L/360)$	8.54	Pass
		Total Load $(D+L)$	25.00 $(L/240)$	21.71	Pass
	Unlipped channel	Live Load (L)	16.67 $(L/360)$	5.73	Pass
		Total Load $(D+L)$	25.00 $(L/240)$	15.68	Pass
	Built-up I-section	Live Load (L)	16.67 $(L/360)$	7.18	Pass
		Total Load $(D+L)$	25.00 $(L/240)$	19.73	Pass
Girder	Lipped channel	Live Load (L)	16.67 $(L/360)$	6.08	Pass
		Total Load $(D+L)$	25.00 $(L/240)$	15.78	Pass
	Unlipped channel	Live Load (L)	16.67 $(L/360)$	4.35	Pass
		Total Load $(D+L)$	25.00 $(L/240)$	12.15	Pass
	Built-up I-section	Live Load (L)	16.67 $(L/360)$	5.51	Pass
		Total Load $(D+L)$	25.00 $(L/240)$	15.49	Pass

To provide a clearer understanding of the members' behavior, the deflection curves for the optimized lipped channel sections are plotted along the full span. Figure 11 illustrates the deflection of the secondary beam under both live load and total service load. Similarly, Figure 12 shows the deflection curves for the girder under the same load cases. The plots visually confirm that the maximum deflection occurs at the mid-span and remains well within the allowable limits for all cases.

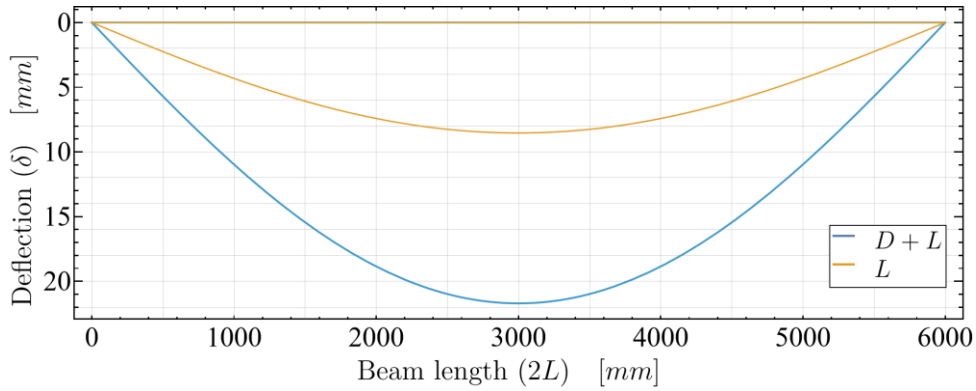

Figure 11:
Deflection curves for the optimized lipped channel secondary beam under live load and total service load

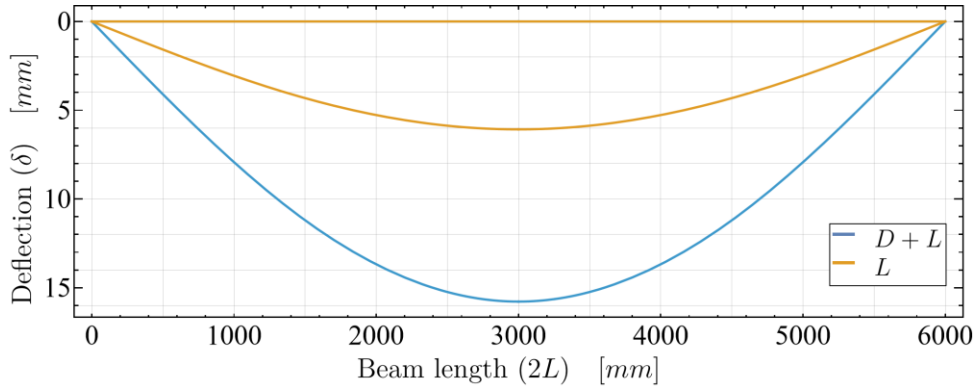

Figure 12:
Deflection curves for the optimized lipped channel girder under live load and total service load

3.2 Analysis of Results

The primary finding from the serviceability analysis is that all six strength-optimized sections successfully satisfy the deflection criteria specified by the IBC. As presented in Table 3, the calculated maximum deflections for both secondary beams and girders are well below the allowable limits for both live load and total load conditions. The initial concern that highly slender, optimized sections might fail deflection checks was not substantiated. Despite the optimization algorithm pushing the designs to the limit of their strength capacity, the resulting sections retained sufficient bending stiffness to control deflections effectively under service loads. This validates the viability of these efficient designs for practical application and demonstrates that a well-executed strength optimization, following the comprehensive limit states in AISI S100-16, can produce profiles that are robust in both strength and serviceability.

A deeper comparative analysis of the results reveals the superior overall efficiency of the lipped channel section. A review of the optimized dimensions in Table 2 shows that the lipped channel section required the smallest cross-section area to meet the strength demands for both the secondary beam (1644.87 mm^2) and the girder (2687.19 mm^2), making it the most materially efficient profile. This is attributed to the edge stiffeners (lips), which provide rotational restraint to the flanges, significantly increasing the section's resistance to local and distortional buckling and allowing for a lighter design.

However, this material efficiency results in a trade-off in terms of stiffness. The deflection data in Table 3 indicates that the lighter, more slender lipped channel section consistently exhibited the largest deflections among the three profiles. For instance, under total load, the

lipped channel section secondary beam deflected 21.71 mm, whereas the heavier unlipped channel and built-up I-section deflected only 15.68 mm and 19.73 mm, respectively. This is an expected outcome, as the lighter profile possesses a lower effective moment of inertia. Nevertheless, it is crucial to note that even these larger deflections were still comfortably within the allowable limit of 25.00 mm.

For designers of cold-formed steel floor systems, these findings indicate that the use of lipped channel sections is a highly effective strategy. It achieves the primary goal of material economy through strength optimization while simultaneously providing robust and compliant performance against deflection. Therefore, it represents the most well-rounded and efficient profile among those studied for both secondary beams and girders.

4. CONCLUSION

This study investigated the deflection performance of three distinct cold-formed steel profiles—a lipped channel, an unlipped channel, and a built-up I-section—after they were sizing-optimized (via parametric scaling) for strength limit states according to AISI S100-16. The primary objective was to verify whether these materially efficient, slender sections, resulting from the strength-based optimization, could satisfy the serviceability limit state of deflection as specified in the IBC. Based on the analysis performed on these profiles for both secondary beams and girders, the following conclusions were drawn:

- The strength-based optimization process, which pushes designs toward their structural limits, did not negatively impact the serviceability performance of the members for the configurations studied.
- All six optimized sections, serving as both secondary beams and girders, demonstrated satisfactory deflection behavior. The calculated maximum deflections under both live load and total service load were found to be well within the allowable limits of $L/360$ and $L/240$ respectively.
- Among the profiles evaluated, the lipped channel section demonstrated the most efficient overall performance. Due to the presence of edge stiffeners, it offers superior resistance to local and distortional buckling. This inherent structural efficiency allows it to meet strength requirements with a lighter and more compact section, which in turn provides sufficient flexural rigidity to effectively control deflection.
- The use of a numerical method that accounts for the variable effective moment of inertia (I_{eff}) along the member's span confirmed that even with reduced stiffness in high-moment regions, the overall deflections remained acceptable.

For structural designers, this study's primary insight is that an aggressive strength-optimization strategy can be pursued without inherently compromising serviceability for typical floor systems. However, the findings also reveal a critical nuance: optimization can shift the governing failure mode from local buckling to combined forces, as observed in the unlipped girder profiles. This suggests that while specifying lipped channel sections is an effective strategy for balancing material economy and robust performance, designers should be aware that optimizing for one criterion can elevate the importance of other, less intuitive limit states.

It should be noted that the optimization methodology employed in this study utilized a uniform scaling factor (α), which constitutes a sizing optimization rather than a comprehensive shape optimization, as discussed in the introduction. This approach scales existing profile typologies rather than allowing independent variation of elements (e.g., web, flange, and lip dimensions). A true shape optimization might yield different slenderness ratios, potentially influencing the relationship between strength optimization and deflection performance observed in these results. This distinction represents a potential limitation and an avenue for future study.

Future work could extend this methodology to include the effects of variable loading patterns, the influence of discrete versus continuous lateral bracing on optimization, and the

performance of perforated or web-stiffened sections. Furthermore, validating the numerical deflection results obtained via the EWM-based conjugate beam method against high-fidelity Finite Element Method simulations would provide an additional layer of verification for these slender, optimized profiles.

CONFLICT OF INTEREST

The authors have no competing interests that could have influenced the research or its presentation.

AUTHOR CONTRIBUTION

All authors contributed to the conceptualization and design of the study, the analysis and interpretation of the data, the drafting of the manuscript, and the critical revision of the content.

REFERENCES

1. AbouHamad, M., & Abu-Hamd, M. (2019). Framework for construction system selection based on life cycle cost and sustainability assessment. *Journal of Cleaner Production*, *241*, 118397. https://doi.org/10.1016/j.jclepro.2019.118397
2. Thirunavukkarasu, K., Kanthasamy, E., Gatheeshgar, P., Poologanathan, K., Rajanayagam, H., Suntharalingam, T., & Dissanayake, M. (2021). Sustainable performance of a modular building system made of built-up cold-formed steel beams. *Buildings*, *11*(10), 460. https://doi.org/10.3390/buildings11100460
3. Liang, H., Roy, K., Fang, Z., & Lim, J. B. P. (2022). A critical review on optimization of cold-formed steel members for better structural and thermal performances. *Buildings*, *12*(1), 34. https://doi.org/10.3390/buildings12010034
4. Sheta, A., Ma, X., Zhuge, Y., ElGawady, M. A., Mills, J. E., Singh, A., & Abd-Elaal, E.-S. (2021). Structural performance of novel thin-walled composite cold-formed steel/PE-ECC beams. *Thin-Walled Structures*, *162*, 107586. https://doi.org/10.1016/j.tws.2021.107586
5. Marrone, G., Imperadori, M., & Sesana, M. M. (2023). Life-cycle assessment of light steel frame buildings: A systematic literature review. In *Life-Cycle of Structures and Infrastructure Systems* (pp. 2405–2412). CRC Press. https://doi.org/10.1201/9781003323020-293
6. Tavares, V., Soares, N., Raposo, N., Marques, P., & Freire, F. (2021). Prefabricated versus conventional construction: Comparing life-cycle impacts of alternative structural materials. *Journal of Building Engineering*, *41*, 102705. https://doi.org/10.1016/j.jobe.2021.102705
7. Lawson, R. M., & Richards, J. (2010). Modular design for high-rise buildings. *Proceedings of the Institution of Civil Engineers - Structures and Buildings*, *163*(3), 151–164. https://doi.org/10.1680/stbu.2010.163.3.151
8. Schafer, B. W. (2011). Cold-formed steel structures around the world. *Steel Construction*, *4*(3), 141–149. https://doi.org/10.1002/stco.201110019
9. Rukavina, M. J., Skejić, D., Kralj, A., Ščapec, T., & Milovanović, B. (2022). Development of lightweight steel framed construction systems for nearly-zero energy buildings. *Buildings*, *12*(7), 929. https://doi.org/10.3390/buildings12070929
10. Ádány, S., & Schafer, B. W. (2008). A full modal decomposition of thin-walled, single-branched open cross-section members via the constrained finite strip method. *Journal of Constructional Steel Research*, *64*(1), 12–29. https://doi.org/10.1016/j.jcsr.2007.04.004

11. Peng, Z., Yang, Y., Zhang, L., Xiong, W., & Cai, Y. (2025). A review on the buckling behavior of cold-formed thin-walled steel members. *Mechanics of Solids*, *60*(2), 1469–1484. https://doi.org/10.1134/S0025654425600710

12. Ayhan, D., & Schafer, B. W. (2015). Cold-formed steel member bending stiffness prediction. *Journal of Constructional Steel Research*, *115*, 148–159. https://doi.org/10.1016/j.jcsr.2015.07.004

13. Rasmussen, K. J. R. (2023). Stiffness reduction of cold-formed steel structures subject to sectional buckling and yielding. *Journal of Structural Engineering*, *149*(11). https://doi.org/10.1061/JSENDH.STENG-12655

14. Mojtabaei, S. M., Hajirasouliha, I., & Becque, J. (2021a). Optimized design of cold-formed steel elements for serviceability and ultimate limit states. *Ce/Papers*, *4*(2–4), 481–486. https://doi.org/10.1002/cepa.1319

15. Mojtabaei, S. M., Ye, J., & Hajirasouliha, I. (2019). Development of optimum cold-formed steel beams for serviceability and ultimate limit states using Big Bang-Big Crunch optimisation. *Engineering Structures*, *195*, 172–181. https://doi.org/10.1016/j.engstruct.2019.05.089

16. Gossen, P. A. (n.d.). *Stiffness versus strength*. https://www.structuremag.org/article/stiffness-versus-strength/

17. Lim, J. B. P., & Nethercot, D. A. (2003). Serviceability design of a cold-formed steel portal frame having semi-rigid joints. *Steel and Composite Structures*, *3*(6), 451–474. https://doi.org/10.12989/scs.2003.3.6.451

18. Phan, D. T., Lim, J. B. P., Tanyimboh, T. T., Lawson, R. M., Xu, Y., Martin, S., & Sha, W. (2013). Effect of serviceability limits on optimal design of steel portal frames. *Journal of Constructional Steel Research*, *86*, 74–84. https://doi.org/10.1016/j.jcsr.2013.03.001

19. Ye, J., Hajirasouliha, I., Becque, J., & Pilakoutas, K. (2016a). Development of more efficient cold-formed steel channel sections in bending. *Thin-Walled Structures*, *101*, 1–13. https://doi.org/10.1016/j.tws.2015.12.021

20. Leng, J., Guest, J. K., & Schafer, B. W. (2011). Shape optimization of cold-formed steel columns. *Thin-Walled Structures*, *49*(12), 1492–1503. https://doi.org/10.1016/j.tws.2011.07.009

21. Parastesh, H., Mohammad Mojtabaei, S., Taji, H., Hajirasouliha, I., & Bagheri Sabbagh, A. (2021). Constrained optimization of anti-symmetric cold-formed steel beam-column sections. *Engineering Structures*, *228*, 111452. https://doi.org/10.1016/j.engstruct.2020.111452

22. Parastesh, H., Hajirasouliha, I., Taji, H., & Bagheri Sabbagh, A. (2019). Shape optimization of cold-formed steel beam-columns with practical and manufacturing constraints. *Journal of Constructional Steel Research*, *155*, 249–259. https://doi.org/10.1016/j.jcsr.2018.12.031

23. Mojtabaei, S. M., Becque, J., & Hajirasouliha, I. (2021b). Structural size optimization of single and built-up cold-formed steel beam-column members. *Journal of Structural Engineering*, *147*(4). https://doi.org/10.1061/(ASCE)ST.1943-541X.0002987

24. Ye, J., Hajirasouliha, I., Becque, J., & Eslami, A. (2016b). Optimum design of cold-formed steel beams using Particle Swarm Optimisation method. *Journal of Constructional Steel Research*, *122*, 80–93. https://doi.org/10.1016/j.jcsr.2016.02.014

25. Fourie, P. C., & Groenwold, A. A. (2002). The particle swarm optimization algorithm in size and shape optimization. *Structural and Multidisciplinary Optimization*, *23*(4), 259–267. https://doi.org/10.1007/s00158-002-0188-0

26. Gatheeshgar, P., Poologanathan, K., Gunalan, S., Nagaratnam, B., Tsavdaridis, K. D., & Ye, J. (2020). Structural behaviour of optimized cold-formed steel beams. *Steel Construction*, *13*(4), 294–304. https://doi.org/10.1002/stco.201900024

27. Svanberg, K. (1987). The method of moving asymptotes—a new method for structural optimization. *International Journal for Numerical Methods in Engineering*, *24*(2), 359–373. https://doi.org/10.1002/nme.1620240207

28. Phan, D. T., Mojtabaei, S. M., Hajirasouliha, I., Ye, J., & Lim, J. B. P. (2020). Coupled element and structural level optimisation framework for cold-formed steel frames. *Journal of Constructional Steel Research*, *168*, 105867. https://doi.org/10.1016/j.jcsr.2019.105867

29. Akchurin, D., Ding, C., Xia, Y., Blum, H., Schafer, B. W., & Li, Z. (2022). Optimization of cold-formed steel members considering reduced stiffness and strength due to cross-sectional instabilities. *Proceedings of the Structural Stability Research Council-Proceedings of the 2022 Annual Stability Conference, Denver, CO, USA*, 22–25.

30. Akchurin, D., Ding, C., Xia, Y., Blum, H. B., Schafer, B. W., & Li, Z. (2023). Instability-driven family optimization of cold-formed steel lipped-channel cross-sections with strength and stiffness constraints. *Thin-Walled Structures*, *192*, 111118. https://doi.org/10.1016/j.tws.2023.111118

31. Ayhan, D., & Schafer, B. W. (2012). Characterization of moment-rotation response of cold-formed steel beams. *Annual Stability Conference, Structural Stability Research Council*.

32. American Iron and Steel Institute. (2022). *North American specification for the design of cold-formed steel structural members (AISI S100-16 (2020) w/S3-22)*. https://www.buildusingsteel.org/wp-content/uploads/2023/06/AISI-S100-16-2020-wS3-22.pdf

33. Mahar, A. M., Jayachandran, S. A., & Mahendran, M. (2022). Design of locally buckling cold-formed steel built-up columns formed by unlipped channel sections. *Thin-Walled Structures*, *174*, 109132. https://doi.org/10.1016/j.tws.2022.109132

34. Schafer, B. W. (2019). Advances in the direct strength method of cold-formed steel design. *Thin-Walled Structures*, *140*, 533–541. https://doi.org/10.1016/j.tws.2019.03.001

35. Phan, D. K., & Rasmussen, K. J. R. (2019). Flexural rigidity of cold-formed steel built-up members. *Thin-Walled Structures*, *140*, 438–449. https://doi.org/10.1016/j.tws.2019.03.051

36. Deng, F., He, Y., Deng, L., & Zhong, W. (2022). Experimental and numerical study on the flexural behavior of cold-formed steel multi-limb built-up section beams. *Buildings*, *12*(10), 1639. https://doi.org/10.3390/buildings12101639

37. Rasmussen, K. J. R., Khezri, M., Zhang, H., & Schafer, B. W. (2025). Recent research on built-up cold-formed steel structures. *Thin-Walled Structures*, *215*, 113546. https://doi.org/10.1016/j.tws.2025.113546

38. Ananthi, G. B. G., Srivardhini, M. S., & Deepak, M. S. (2024). *Optimization of cold-formed steel perforated sections subjected to bending* (pp. 343–361). https://doi.org/10.1007/978-3-031-72527-2_27

39. Abdel-Rahman, N., & Sivakumaran, K. S. (1998). Effective design width for perforated cold-formed steel compression members. *Canadian Journal of Civil Engineering*, *25*(2), 319–330. https://doi.org/10.1139/cjce-25-2-319

40. International Codes Council. (2018). *International Building Code*. https://www.iccsafe.org/products-and-services/i-codes/2018-i-codes/ibc/

41. American Society for Testing and Materials. (2019). *Standard specification for carbon structural steel (ASTM A36/A36M-19)*. https://store.astm.org/a0036_a0036m-19.html

42. İnşaat Mühendisleri Odası. (2017). *Yapı malzemeleri ve yapı kısımlarının birim hacim ağırlıkları* [Unit volume weights of building materials and building parts]. https://www.imo.org.tr/resimler/dosya_ekler/f7deb880ca6b4b7_ek.pdf

43. Özçe Demir Çelik. (2014). *Galvanizli / trapez sac boyutları ve ağırlıkları* [Galvanized / trapezoidal sheet dimensions and weights]. https://www.ozcedemir.com.tr/galvanizli_saclar-s59.html

44. Celep, Z. (2022). *Betonarme yapılar* [Reinforced concrete structures] (12th ed.). Zekai Celep.

45. Türk Standartları Enstitüsü. (2024). *Yapı elemanlarının boyutlandırılmasında alınacak yüklerin hesap değerleri (TS 498/T3)* [Calculation values of loads to be taken in the dimensioning of building elements (TS 498/T3)]. https://intweb.tse.org.tr/Standard/Standard/Standard.aspx?081118051115108051104119110104055047105102120088111043113104073100097112047071071086090066043110

46. American Society of Civil Engineers. (2022). *Minimum design loads and associated criteria for buildings and other structures (ASCE/SEI 7-22)*. https://ascelibrary.org/doi/book/10.1061/9780784415788

47. Bischoff, P. H. (2005). Reevaluation of Deflection Prediction for Concrete Beams Reinforced with Steel and Fiber Reinforced Polymer Bars. *Journal of Structural Engineering*, *131*(5), 752–767. https://doi.org/10.1061/(ASCE)0733-9445(2005)131:5(752)

APPENDIX A

Table A1. Calculated effective moments of inertia for secondary beams [mm^4]

	Lipped channel		Unlipped channel		Built-up I-section	
Node #	*L*	*D* + *L*	*L*	*D* + *L*	*L*	*D* + *L*
1	2.9049E+07	2.9049E+07	4.3558E+07	4.3558E+07	3.4789E+07	3.4789E+07
3	2.9049E+07	2.9049E+07	4.3558E+07	4.3558E+07	3.4789E+07	3.4789E+07
5	2.9049E+07	2.9049E+07	4.3558E+07	4.3558E+07	3.4789E+07	3.4789E+07
7	2.9049E+07	2.9049E+07	4.3558E+07	4.3558E+07	3.4789E+07	3.4789E+07
9	2.9049E+07	2.9049E+07	4.3558E+07	4.3558E+07	3.4789E+07	3.4789E+07
11	2.9049E+07	2.9049E+07	4.3558E+07	4.3313E+07	3.4789E+07	3.4592E+07
13	2.9049E+07	2.9049E+07	4.3558E+07	4.2780E+07	3.4789E+07	3.4166E+07
15	2.9049E+07	2.9049E+07	4.3558E+07	4.2324E+07	3.4789E+07	3.3802E+07
17	2.9049E+07	2.9049E+07	4.3558E+07	4.1933E+07	3.4789E+07	3.3489E+07
19	2.9049E+07	2.9049E+07	4.3558E+07	4.1595E+07	3.4789E+07	3.3220E+07
21	2.9049E+07	2.9049E+07	4.3558E+07	4.1303E+07	3.4789E+07	3.2986E+07
23	2.9049E+07	2.9049E+07	4.3558E+07	4.1049E+07	3.4789E+07	3.2783E+07
25	2.9049E+07	2.9049E+07	4.3558E+07	4.0827E+07	3.4789E+07	3.2606E+07
27	2.9049E+07	2.9000E+07	4.3558E+07	4.0633E+07	3.4789E+07	3.2451E+07
29	2.9049E+07	2.8947E+07	4.3558E+07	4.0464E+07	3.4789E+07	3.2316E+07

Table A1. (continued)

	Lipped channel		Unlipped channel		Built-up I-section	
Node #	L	$D+L$	L	$D+L$	L	$D+L$
31	2.9049E+07	2.8900E+07	4.3558E+07	4.0316E+07	3.4789E+07	3.2198E+07
33	2.9049E+07	2.8857E+07	4.3459E+07	4.0188E+07	3.4722E+07	3.2096E+07
35	2.9049E+07	2.8820E+07	4.3361E+07	4.0034E+07	3.4644E+07	3.1972E+07
37	2.9049E+07	2.8788E+07	4.3276E+07	3.9874E+07	3.4576E+07	3.1844E+07
39	2.9049E+07	2.8760E+07	4.3203E+07	3.9737E+07	3.4518E+07	3.1734E+07
41	2.9049E+07	2.8737E+07	4.3142E+07	3.9623E+07	3.4469E+07	3.1643E+07
43	2.9049E+07	2.8718E+07	4.3093E+07	3.9531E+07	3.4430E+07	3.1569E+07
45	2.9049E+07	2.8704E+07	4.3055E+07	3.9459E+07	3.4400E+07	3.1512E+07
47	2.9049E+07	2.8693E+07	4.3028E+07	3.9408E+07	3.4378E+07	3.1472E+07
49	2.9049E+07	2.8687E+07	4.3011E+07	3.9378E+07	3.4365E+07	3.1448E+07
51	2.9049E+07	2.8685E+07	4.3006E+07	3.9368E+07	3.4361E+07	3.1440E+07

Table A2. Calculated effective moments of inertia for girders [mm^4]

	Lipped channel		Unlipped channel		Built-up I-section	
Node #	L	$D+L$	L	$D+L$	L	$D+L$
1	7.7529E+07	7.7529E+07	1.0889E+08	1.0889E+08	8.5894E+07	8.5894E+07
3	7.7529E+07	7.7529E+07	1.0889E+08	1.0889E+08	8.5894E+07	8.5894E+07
5	7.7529E+07	7.7529E+07	1.0889E+08	1.0889E+08	8.5894E+07	8.5894E+07
7	7.7529E+07	7.7529E+07	1.0889E+08	1.0889E+08	8.5894E+07	8.5894E+07
9	7.7529E+07	7.7529E+07	1.0889E+08	1.0889E+08	8.5894E+07	8.5894E+07
11	7.7529E+07	7.7529E+07	1.0889E+08	1.0889E+08	8.5894E+07	8.5894E+07
13	7.7529E+07	7.7529E+07	1.0889E+08	1.0804E+08	8.5894E+07	8.5160E+07
15	7.7529E+07	7.7529E+07	1.0889E+08	1.0675E+08	8.5894E+07	8.4138E+07
17	7.7529E+07	7.7529E+07	1.0889E+08	1.0558E+08	8.5894E+07	8.3219E+07
19	7.7529E+07	7.7529E+07	1.0889E+08	1.0453E+08	8.5894E+07	8.2392E+07
21	7.7529E+07	7.7529E+07	1.0889E+08	1.0359E+08	8.5894E+07	8.1645E+07
23	7.7529E+07	7.7529E+07	1.0889E+08	1.0273E+08	8.5894E+07	8.0966E+07
25	7.7529E+07	7.7529E+07	1.0889E+08	1.0194E+08	8.5894E+07	8.0347E+07
27	7.7529E+07	7.7496E+07	1.0889E+08	1.0145E+08	8.5894E+07	7.9960E+07
29	7.7529E+07	7.7419E+07	1.0889E+08	1.0121E+08	8.5894E+07	7.9771E+07
31	7.7529E+07	7.7343E+07	1.0889E+08	1.0098E+08	8.5894E+07	7.9588E+07
33	7.7529E+07	7.7267E+07	1.0889E+08	1.0075E+08	8.5894E+07	7.9411E+07
35	7.7529E+07	7.7192E+07	1.0888E+08	1.0054E+08	8.5856E+07	7.9238E+07
37	7.7529E+07	7.7119E+07	1.0870E+08	1.0030E+08	8.5709E+07	7.9013E+07
39	7.7529E+07	7.7046E+07	1.0851E+08	9.9958E+07	8.5565E+07	7.8739E+07
41	7.7529E+07	7.6974E+07	1.0833E+08	9.9617E+07	8.5422E+07	7.8470E+07
43	7.7529E+07	7.6903E+07	1.0815E+08	9.9282E+07	8.5282E+07	7.8205E+07
45	7.7529E+07	7.6833E+07	1.0798E+08	9.8951E+07	8.5143E+07	7.7944E+07
47	7.7529E+07	7.6764E+07	1.0780E+08	9.8627E+07	8.5005E+07	7.7687E+07
49	7.7529E+07	7.6695E+07	1.0763E+08	9.8307E+07	8.4870E+07	7.7435E+07